

Revisiting Cross-View Localization from Image Matching

Panwang Xia¹ Qiong Wu¹ Lei Yu² Yi Liu¹ Mingtao Xiong¹
Lei Liang² Yongjun Zhang¹ Yi Wan¹
¹Wuhan University ²AntGroup
{yi.wan}@whu.edu.cn

Abstract

Cross-view localization aims to estimate the 3 degrees of freedom pose of a ground-view image by registering it to aerial or satellite imagery. It is essential in GNSS-denied environments such as urban canyons and disaster zones. Existing methods either regress poses directly or align features in a shared bird’s-eye view (BEV) space, both built upon accurate spatial correspondences between perspectives. However, these methods fail to establish strict cross-view correspondences, yielding only coarse or geometrically inconsistent matches. Consequently, fine-grained image matching between ground and aerial views remains an unsolved problem, which in turn constrains the interpretability of localization results. In this paper, we revisit cross-view localization from the perspective of cross-view image matching and propose a novel framework that improves both matching and localization. Specifically, we introduce a Surface Model to model visible regions for accurate BEV projection, and a SimRefiner module to refine the similarity matrix through local-global residual correction, eliminating the reliance on post-processing like RANSAC. To further support research in this area, we introduce CVFM, the first benchmark with 32,509 cross-view image pairs annotated with pixel-level correspondences. Extensive experiments demonstrate that our approach substantially improves both localization accuracy and image matching quality, setting new baselines under extreme view-point disparity.

1. Introduction

Cross-view localization aims to estimate the 3 degrees of freedom (3-DoF) pose of a ground-view image by aligning it with aerial or satellite imagery, where the output typically includes the location and yaw orientation. This task is essential for visual positioning in GNSS-denied environments, such as urban canyons and post-disaster areas. Applications span autonomous navigation [12], urban planning [35], and emergency response [9].

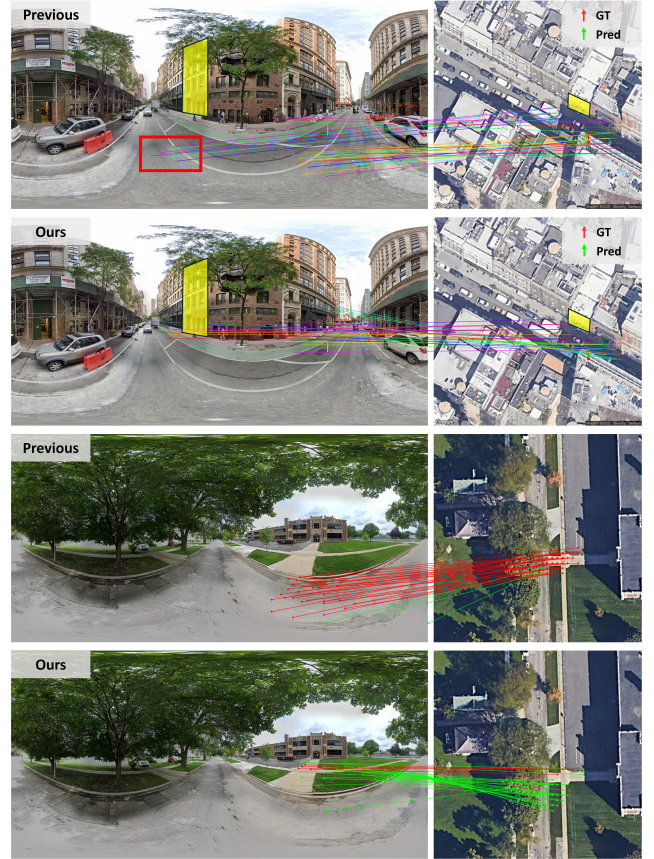


Figure 1. The top two rows show localization results, with a shared region highlighted in yellow across views; the red box in the top-left image marks a mismatch from the previous method. The bottom two rows show matching results, where green and red lines indicate correct and incorrect matches. Our method estimates surface height from the ground view, enabling physically consistent cross-view image matching and more accurate localization.

To tackle this problem, existing methods follow two major directions. The first retains the native ground-view perspective, directly regressing the camera pose from cross-view pairs via slice- or split-based representations to encode

structural priors and learn spatial correspondences [7, 31, 32, 37]. The second maps both views into a shared space, such as bird’s-eye view (BEV), where geometric alignment is more tractable [19, 21, 25, 30]. Despite these differences, all these approaches fundamentally rely on robust spatial correspondences under extreme viewpoint changes: for the first category, matching quality directly dictates localization accuracy; for the second, it is embedded in BEV feature construction. Thus, improving cross-view image matching is not only for matching itself but also for boosting localization performance.

Image matching defines how one view can be interpreted from another, and is a cornerstone for tasks such as scene reconstruction, view synthesis, and cross-modal representation learning. In the cross-view setting, effective image matching not only improves localization accuracy, but also contributes to broader cross-view understanding by enabling semantic and geometric integration across perspectives. However, existing matching methods [2, 4, 8, 15, 22, 24], though successful in standard image-pair settings, often struggle to handle the extreme appearance and viewpoint variations between ground and aerial images.

In this work, we revisit cross-view localization from the perspective of image matching. We propose to simultaneously enhance cross-view localization and enable cross-view image matching, thereby contributing to a unified understanding across drastically different perspectives. Building upon prior BEV-based localization frameworks, we design a novel architecture with two key components: (i) We propose a Surface Model Mechanism that explicitly estimates the visible surface from the ground-view image via volumetric feature accumulation. This surface estimation enables the network to extract features from geometrically valid and visually consistent regions, avoiding sampling from sky or underground areas. As a result, the constructed BEV features are both semantically meaningful and spatially accurate. (ii) Second, we introduce SimRefiner, a learnable refinement module that enhances the BEV-level similarity matrix through a dual-branch residual correction mechanism, jointly modeling local spatial patterns and global correspondence structures. SimRefiner enables robust pose estimation by suppressing mismatches and reinforcing geometric consistency without the heavy time cost of post-processing methods like RANSAC. Moreover, the refined similarity distribution further improves the quality of cross-view image matching. Together, these modules enhance the interpretability and robustness of cross-view feature alignment, leading to improved 3-DoF localization performance and stronger image-level correspondence.

Despite the importance of cross-view image matching, it remains underexplored in existing benchmarks. To address this gap, we introduce the first dataset tailored for ground-

to-satellite matching: the Cross-View Fine-Grained Image Match (CVFM) dataset. CVFM is constructed by sampling ground-view images from the DReSS dataset [29], and generating dense pixel-level correspondences by projecting ground-view pixels onto aerial-view images using ground-truth depth maps from the DReSS-D [37] dataset. To ensure label quality, we further manually select a high-fidelity subset to serve as a reliable benchmark. CVFM contains 32,509 high-quality cross-view image pairs for evaluating image matching algorithms under extreme viewpoint disparities, and facilitates future research in geometry-aware cross-view understanding. To summarize, our main contributions are as follows:

- We revisit cross-view localization from the perspective of cross-view image matching, and propose a unified framework that enhances both localization and image matching under drastic viewpoint differences.
- We introduce a Surface Model Mechanism that explicitly models the visible surface geometry from the ground-view image via volumetric feature accumulation, enabling semantically and geometrically consistent BEV representations.
- We design SimRefiner, a learnable similarity refinement module that jointly models local spatial coherence and global correspondence trends, leading to robust pose estimation without additional inference overhead.
- We present the CVFM dataset, the first benchmark dedicated to pixel-level ground-to-satellite image matching, offering a new testbed for evaluating matching methods under extreme cross-view conditions.

2. Related work

Cross-View Localization has traditionally been approached as a large-scale image retrieval problem [3, 17, 26–29], where the goal is to identify the most visually similar satellite-view image for a given ground-view image. More recently, research has shifted toward fine-grained estimation of the camera’s spatial pose, enabling more precise localization beyond coarse retrieval [6, 7, 16, 18–21, 25, 30–33, 37].

A major challenge in cross-view localization lies in the drastic viewpoint differences between ground and satellite imagery. One prominent line of work addresses this issue by directly regressing the 3-DoF pose (location and orientation) of the ground-view image using deep neural networks trained on cross-view image pairs [7, 31, 32, 37]. These methods implicitly learn spatial correspondences and can exploit the full visual content, but they require the network to effectively model complex and diverse urban scenes. An alternative and increasingly popular approach leverages a shared representation in the form of Bird’s Eye View (BEV), which captures a co-visible geometry between the ground and satellite views [6, 19, 21, 25]. By trans-

forming ground-view into the BEV space, the model can alleviate the extreme viewpoint gap. However, BEV representations also introduce challenges: ground images often suffer from occlusions caused by buildings and vegetation, while the BEV-transformed images may contain distortions or lose important visual cues. Recent advances [30] have attempted to mitigate these issues by learning adaptive or view-aware BEV embeddings, aiming to preserve semantic consistency while maintaining the advantages of viewpoint alignment.

Image Matching under Extreme Viewpoint Changes is a highly related task, and can be viewed as a subproblem of general image matching. Traditional matching algorithms [4, 15, 22] perform well when the viewpoint variation is small, such as matching different views of the same building from the ground. However, their performance degrades significantly when the images are captured from drastically different perspectives, such as ground versus satellite views. Recent advances [2, 8, 24] have introduced hybrid pipelines that jointly estimate point clouds alongside feature matching. These methods leverage the predicted 3D geometry to provide additional spatial cues, significantly improving matching robustness under large viewpoint changes. Furthermore, efforts [23] to expand existing datasets to include ground-aerial image pairs have shown to substantially enhance model performance on cross-view matching benchmarks.

Our method enables coarse ground-aerial image matching using only 3-DoF supervision during training, which is readily available in practice. The resulting coarse correspondences provide strong priors for downstream fine-grained matching and can significantly improve performance under extreme viewpoint changes.

3. Methodology

Given a ground-view image I_{grd} and an aerial-view image I_{sat} that spatially covers the location of the ground camera, our objective is to estimate the accurate 3-DoF pose $p = [\text{translation}, \text{orientation}]$, where the translation denotes the camera location in pixel coordinates on I_{sat} , and the orientation represents the yaw angle of the ground-view camera.

3.1. Motivation and Overview

Motivation. Recent works such as FG2 [30] estimate 3-DoF camera pose by establishing cross-view correspondences in BEV space, constructing learnable BEV features via deformable attention for patch-level alignment across extreme viewpoint changes. However, correspondence reliability is limited by geometric ambiguities in ground-view BEV construction, where inaccurate feature sampling and projection often yield semantically inconsistent matches and degrade localization accuracy.

(i) Ground-view BEV construction projects 3D sampling points of varying heights into the ground-view image plane, requiring identification of the true visible surface along each vertical ray. Prior methods heuristically pick the height layer with the maximum attention weight, lacking physical grounding and often selecting incorrect layers (e.g., -10 m, see Fig. 5a), which aggregates features from semantically wrong regions. We propose a Surface Model Mechanism that adaptively estimates surface location via bottom-up accumulation of height-wise attention and thresholded volumetric integration, inspired by volume rendering [5, 11, 13, 36]. This yields physically consistent surfaces and ensures deformable attention focuses on meaningful regions in the ground image.

(ii) Prior methods employ a RANSAC-based post-processing step to filter mismatches in the similarity matrix, which, while effective, incurs nearly $30\times$ runtime overhead [30] and exposes a deeper issue: the matrix itself contains high-scoring outliers that degrade matching reliability. To address this, we propose SimRefiner, a dedicated refinement module that explicitly models both local patch structures and the global similarity distribution to suppress mismatches at the source.

Overview. We start by extracting image-space features f_{grd} and f_{sat} using a frozen DINOv2 [14] backbone, followed by view-specific encoders to project them into BEV space. For the ground view, a 3D voxel grid is constructed around the camera, and deformable attention samples multi-scale features across vertical layers, producing a volumetric BEV tensor $\xi_{\text{grd}}^{3D} \in \mathbb{R}^{M \times N \times N \times C}$. Our Surface Model (Sec. 3.2) then estimates the visible surface and aggregates valid height-wise features into a compact BEV map $f_{\text{grd}}^{\text{bev}} \in \mathbb{R}^{N \times N \times c}$. For the aerial view, features are directly sampled onto a 2D BEV grid ξ_{sat} and projected into $f_{\text{sat}}^{\text{bev}}$. We compute a dense similarity matrix via scaled dot-product and refine it with SimRefiner (Sec. 3.3), which combines local convolution and global context modeling to suppress mismatches. High-confidence matches are fed into a weighted Procrustes solver to recover the 3-DoF pose $P_{\text{pred}} = [R, T]$.

Training is end-to-end with three losses (Sec. 3.4): virtual correspondence error \mathcal{L}_{VCE} , matching loss \mathcal{L}_{M} , and height consistency loss $\mathcal{L}_{\text{height}}$, jointly optimizing feature alignment, pose estimation, and surface prediction.

3.2. Surface Model Mechanism

To accurately project ground-view image features into the BEV domain, it is essential to determine from which height level each BEV cell should gather information. We propose a *Surface Model Mechanism* to explicitly estimate the visible surface height at each BEV cell, thereby improving the geometric validity and semantic consistency of ground-view BEV features.

Ground-view BEV encoding. We follow prior

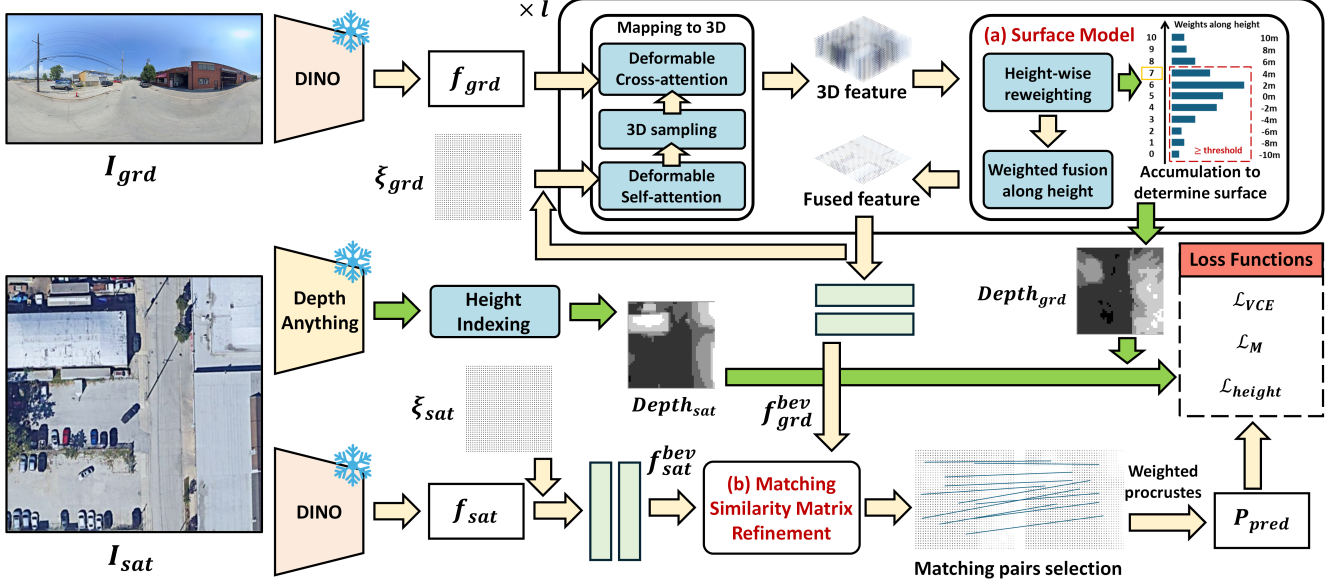


Figure 2. Overview of our framework and loss functions. ξ_{grd} and ξ_{sat} denote BEV point sets for ground-view and aerial-view features. During BEV encoding, (a) the Surface Model physically estimates surface height from the ground-view, supervised by a pseudo-height map derived from the aerial-view. During matching, (b) the Matching Similarity Matrix Refinement module (SimRefiner) refines similarity scores to suppress mismatches and improve correspondence reliability.

works [10, 30] to build a uniform 3D voxel grid centered at the ground camera. Each voxel corresponds to a sampling point (x, y, z) , where the height z is discretized into M layers (e.g., $M = 11$, covering $[-10\text{ m}, 10\text{ m}]$). For each voxel, we use deformable attention [39] to project it into the ground-view feature map f_{grd} , retrieving visual features and aggregating them into a volumetric BEV tensor $\xi_{grd}^{3D} \in \mathbb{R}^{M \times N \times N \times C}$.

Instead of selecting the height index with maximum activation, we introduce a volume rendering-style accumulation strategy to infer the most likely surface layer. Specifically, we learn a per-voxel confidence score along the height axis and compute a cumulative sum from bottom to top. The surface layer is determined as the first index where the cumulative score exceeds a threshold. The final ground-view BEV feature $f_{grd}^{bev} \in \mathbb{R}^{N \times N \times c}$ is then obtained by a weighted fusion of features along the height dimension, followed by a projection head.

Aerial-view BEV encoding and height indexing. For the aerial-view image, which is already captured from a top-down perspective, we directly sample features onto a 2D BEV grid ξ_{sat} using the known ground sampling distance (GSD), and then apply a lightweight projection to obtain $f_{sat}^{bev} \in \mathbb{R}^{N \times N \times c}$.

In addition, we leverage a pretrained lightweight monocular depth estimator (DepthAnything v2-small [34]) to predict a depth map $depth_{sat}$ from the aerial image. Since the predicted depth from the aerial-view image lacks ab-

solute metric scale, we adopt a simple yet effective scene prior: the ground is assumed to be approximately planar and the ground-view camera is mounted at a typical height of 2–3 m. Under this prior, we anchor the minimum value in the aerial-view depth prediction $depth_{sat}$ to -3 m , which we treat as the ground level relative to the camera. The remaining relative depth values are then linearly scaled to approximate real-world heights, which are discretized into indices aligned with our height sampling grid. Although this mapping is inherently approximate due to uncertainties in depth estimation and variations in real-world camera placement, it nonetheless provides a useful pseudo-supervision signal to guide the ground-view surface prediction $depth_{grd}$. This supervision guides the Surface Model Mechanism to learn semantically meaningful and spatially grounded height representations.

Overall, our Surface Model Mechanism enables accurate and learnable height modeling during BEV construction, ensuring that ground-view features are sampled from geometrically credible regions and improving cross-view feature alignment.

3.3. Matching Similarity Matrix Refinement

To address the limitations of post-processing strategies, we introduce *SimRefiner*, a residual correction module designed to refine the matching similarity matrix by modeling both local spatial structures and global correspondence patterns.

Initial similarity matrix. Given the ground-view and aerial-view BEV features $f_{\text{grd}}^{\text{bev}}, f_{\text{sat}}^{\text{bev}} \in \mathbb{R}^{N \times N \times c}$, we flatten them into sequences of patches and compute the initial similarity matrix via scaled cosine similarity:

$$S_{\text{orig}} = \frac{F_{\text{grd}}^{\text{bev}} \cdot F_{\text{sat}}^{\text{bev}^\top}}{\tau} \in \mathbb{R}^{N^2 \times N^2}, \quad (1)$$

where τ is a temperature hyperparameter, and $F_{\text{grd}}^{\text{bev}}, F_{\text{sat}}^{\text{bev}} \in \mathbb{R}^{N^2 \times c}$ denote the flattened BEV features. Each row in S_{orig} represents the similarity scores between one ground-view patch and all N^2 aerial-view patches.

Dual-branch residual correction. We design a dual-branch refinement module that captures both local spatial consistency and global matching trends.

(i) Local refinement. We reshape S_{orig} into a 3D similarity cube $S_{\text{cube}} \in \mathbb{R}^{N \times N \times N^2}$, where each ground-view spatial position stores a full similarity vector over aerial-view locations. A 3-layer 3D convolutional network is applied to extract spatially-aware residuals:

$$\Delta_{\text{local}} = \text{Conv3D}(S_{\text{cube}}) \in \mathbb{R}^{N^2 \times N^2}. \quad (2)$$

(ii) Global refinement. In parallel, a row-wise MLP is applied to S_{orig} to capture global correspondence patterns:

$$\Delta_{\text{global}} = \text{MLP}(S_{\text{orig}}) \in \mathbb{R}^{N^2 \times N^2}. \quad (3)$$

Residual fusion and ratio gating. The local and global correction terms are summed to form the residual $\Delta = \Delta_{\text{local}} + \Delta_{\text{global}}$. A ratio gating vector $\alpha \in [0, 1]^{N^2}$, predicted by a lightweight MLP and broadcast across rows, adaptively modulates this residual. The refined similarity matrix is thus:

$$S_{\text{refined}} = S_{\text{orig}} + \alpha \cdot (\Delta_{\text{local}} + \Delta_{\text{global}}), \quad (4)$$

where \cdot denotes row-wise element-wise multiplication.

Adaptive dustbin. To handle unmatched patches, we extend the matrix with a learnable dustbin row and column:

$$S_{\text{dustbin}} = \begin{bmatrix} S_{\text{refined}} & \mathbf{b}_{\text{col}} \\ \mathbf{b}_{\text{row}}^\top & b_\theta \end{bmatrix} \in \mathbb{R}^{(N^2+1) \times (N^2+1)}. \quad (5)$$

We then apply doubly-stochastic normalization via row-wise and column-wise softmax:

$$S = [\text{Softmax}_{\text{row}}(S_{\text{dustbin}}) \cdot \text{Softmax}_{\text{col}}(S_{\text{dustbin}})]_{1:N^2, 1:N^2}, \quad (6)$$

where $S \in \mathbb{R}^{N^2 \times N^2}$ is the final refined similarity matrix used for patch correspondence and downstream pose estimation.

3.4. Loss Functions

Our framework is trained end-to-end using a weighted combination of three losses: a Virtual Correspondence Error (VCE) loss \mathcal{L}_{VCE} that supervises the predicted 3-DoF pose, a matching loss \mathcal{L}_{M} that enforces patch-wise alignment in BEV space, and a height consistency loss $\mathcal{L}_{\text{height}}$ that regularizes the predicted surface. The overall loss is:

$$\mathcal{L} = \mathcal{L}_{\text{VCE}} + \beta_1 \cdot \mathcal{L}_{\text{M}} + \beta_2 \cdot \mathcal{L}_{\text{height}}, \quad (7)$$

where β_1 and β_2 are weighting hyperparameters.

Virtual Correspondence Error (VCE). To supervise the predicted relative pose $P_{\text{pred}} = [R, T]$, we adopt the Virtual Correspondence Error proposed in [1]. We define a set of uniformly sampled 2D query points $\{pts_i\}_{i=1}^{N_v}$ spanning a square BEV region of size $L_v \times L_v$. These points are projected into the reference frame using both predicted and ground-truth poses, yielding transformed sets $pts_i^{\text{pred}}, pts_i^{\text{gt}}$. The loss minimizes the average Euclidean distance between these projected pairs:

$$\mathcal{L}_{\text{VCE}} = \frac{1}{N_v} \sum_{i=1}^{N_v} \left\| pts_i^{\text{pred}} - pts_i^{\text{gt}} \right\|_2. \quad (8)$$

Matching loss. To directly supervise the similarity matrix, we follow [30] and construct patch correspondences based on the ground-truth pose. For each query patch $n_{\text{grd}} = (x, y)$, we project its BEV location to the reference frame using P_{gt} , obtaining a target patch n'_{sat} . Similarly, each reference patch n_{sat} is back-projected to the query frame to find its counterpart n'_{grd} . We then compute two symmetric InfoNCE losses over the similarity matrix $S_{\text{orig}} \in \mathbb{R}^{N^2 \times N^2}$:

$$\mathcal{L}_{\text{infoNCE}}^{\text{grd} \rightarrow \text{sat}} = -\frac{1}{N_s} \sum_{i=1}^{N_s} \log \left(\frac{e^{S_{\text{orig}} n_{\text{grd}}, n'_{\text{sat}}}}{\sum_{j=1}^{N^2} e^{S_{\text{orig}} n_{\text{grd}}, j}} \right), \quad (9)$$

$$\mathcal{L}_{\text{infoNCE}}^{\text{sat} \rightarrow \text{grd}} = -\frac{1}{N_s} \sum_{i=1}^{N_s} \log \left(\frac{e^{S_{\text{orig}} n'_{\text{grd}}, n_{\text{sat}}}}{\sum_{j=1}^{N^2} e^{S_{\text{orig}} j, n_{\text{sat}}}} \right). \quad (10)$$

The total matching loss is defined as their average:

$$\mathcal{L}_{\text{M}} = \frac{1}{2} \left(\mathcal{L}_{\text{infoNCE}}^{\text{grd} \rightarrow \text{sat}} + \mathcal{L}_{\text{infoNCE}}^{\text{sat} \rightarrow \text{grd}} \right). \quad (11)$$

Height consistency loss. To regularize the height predictions from both modalities, we enforce a consistency loss on corresponding patches. Using the same projected correspondences $n_{\text{grd}} \leftrightarrow n'_{\text{sat}}$, we extract their estimated depths from the ground and aerial surface maps and minimize the L1 distance:

$$\mathcal{L}_{\text{height}} = \frac{1}{N_s} \sum_{i=1}^{N_s} \frac{1}{K} \cdot \left| \text{depth}_{\text{grd}}(n_{\text{grd}}) - \text{depth}_{\text{sat}}(n'_{\text{sat}}) \right|, \quad (12)$$

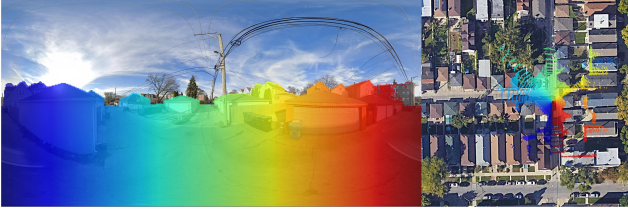


Figure 3. Example illustrating the projection of ground-view pixels onto an aerial-view image, colors denote corresponding points.

where $K = 100$ is a normalization constant that stabilizes training.

4. Experiments

4.1. Datasets and Evaluation Metrics

We evaluate our approach on two public cross-view localization datasets and introduce a new benchmark for fine-grained cross-view image matching:

VIGOR [38] contains ground-view panoramas and aerial-view images collected from four U.S. cities. It supports two experimental settings: (i) *same-area*, where both training and testing samples are drawn from all cities; and (ii) *cross-area*, where training is conducted on two cities and testing on the other two. Since no official validation set is provided, we randomly sample 20% of the training data for validation and use the remaining 80% for training.

DReSS-D [37] is a reprocessed version of DReSS [29], containing aligned ground-view panoramas and aerial-view images from six global cities. It follows the same-area and cross-area evaluation protocols as VIGOR. Similarly, we adopt a 80%-20% training-validation split from the original training data.

CVFM is our newly proposed benchmark for fine-grained cross-view image matching between ground-view and aerial-view images, providing the first dense point-to-point correspondences across views. Images are sourced from DReSS [29], with ground-truth correspondences obtained by projecting 3D points from the ground-view into the aerial-view using DReSS-D [37] depth supervision (see Fig. 3). A 30 m distance threshold is applied to filter ground-view pixels, ensuring projected points remain within aerial coverage; the retained pixels define the **valid region**. To guarantee annotation quality, three master’s students with computer vision backgrounds manually verified all candidate pairs over three weeks. The final benchmark contains 32,509 high-quality image pairs.

Evaluation Metrics: For cross-view localization, we report both mean and median errors in translation and orientation under two configurations: (i) *known orientation*, where ground-view panoramas are aligned northward, and (ii) *unknown orientation*, where the heading is arbitrary. For

Method	$\uparrow@5\text{px}$	$\uparrow@10\text{px}$	$\uparrow@15\text{px}$	valid
mast3r-aerial [23]	0.6%	2.0%	3.5%	0.391
FG2 [30]	0.6%	2.2%	5.0%	0.997
Ours	3.1%	11.7%	24.0%	0.915

Table 1. CVFM cross-view image matching results using the top-30 matches. 1 pixel equals approximately 0.12 m. **Best in bold.**

fine-grained image matching, we measure the success ratio under varying pixel error thresholds. Each method is expected to output a set of matched coordinate pairs, denoted as $[(x_{\text{grd}}, y_{\text{grd}}) \leftrightarrow (x_{\text{sat}}, y_{\text{sat}})]^{N_{\text{mch}}}$. We compute the percentage of correct matches among N_{mch} matches under thresholds of 5, 10, and 15 pixels based on the ground truth projection.

4.2. Implementation Details

On both the VIGOR and DReSS-D datasets, we define 41×41 grid points for ξ_{grd} and ξ_{sat} , uniformly distributed over a $71 \text{ m} \times 71 \text{ m}$ area centered at the camera. Along the vertical axis, we use $M = 11$ height layers ranging from -10 m to 10 m . Following [10, 30], the ground-view BEV encoder is composed of $l = 6$ stacked layers. We set the temperature parameter in Eq. 1 to $\tau = 0.1$. In the loss function (Eq. 7), the weighting coefficients are set to $\beta_1 = \beta_2 = 1$. For the Virtual Correspondence Error loss (Eq. 8), we randomly sample $N_v = 100$ 2D points from a BEV region of size $L_v = 5 \text{ m}$. For the matching loss (Eq. 11) and height loss (Eq. 12), the number of sampled patch pairs is set to $N_s = 1024$. All models are trained using the AdamW optimizer with a learning rate of 1×10^{-4} , a batch size of 48, and run for 100 epochs on 8 NVIDIA V100 GPUs.

4.3. Results on cross-view image matching

Quantitative: We compare our approach with prior methods that claim the ability to match ground-view and aerial-view images. Mast3r-aerial is a fine-tuned version of the original Mast3r model on the aerial-Megadepth dataset [23]. FG2 [30] is a recent cross-view localization framework that also demonstrates potential in cross-view image matching. Both FG2 and our method are trained on the same 80% split of the VIGOR train dataset. Each method is required to output $N_{\text{mch}} = 30$ correspondences, where the last column reports the average ratios of matches falling within the **valid** ground-truth region. The success ratio is computed as the number of correct matches divided by the N_{mch} .

As shown in Tab. 1, our method achieves a clear and consistent advantage over previous approaches across all thresholds. This demonstrates that the proposed surface modeling mechanism substantially improves the geometric validity of ground-view features, leading to more accurate

Orien.	Methods	Same-area				Cross-area			
		↓ Localization (m)		↓ Orientation (°)		↓ Localization (m)		↓ Orientation (°)	
		Mean	Median	Mean	Median	Mean	Median	Mean	Median
Known	SliceMatch [7]	5.18	2.58	-	-	5.53	2.55	-	-
	CCVPE [32]	3.60	1.36	-	-	4.97	1.68	-	-
	DenseFlow [21]	3.03	<u>0.97</u>	-	-	5.01	2.42	-	-
	HC-Net [25]	2.65	1.17	-	-	3.35	1.59	-	-
	FG2 [†] [30]	<u>2.16</u>	1.03	-	-	<u>2.67</u>	<u>1.48</u>	-	-
	Ours	1.92	0.96	-	-	2.27	1.32	-	-
Unknown	SliceMatch [7]	6.49	3.13	25.46	4.71	7.22	3.31	25.97	4.51
	CCVPE [32]	<u>3.74</u>	<u>1.42</u>	12.83	6.62	5.41	1.89	27.78	13.58
	DenseFlow [21]	4.97	1.90	11.20	1.59	7.67	3.67	17.63	<u>2.94</u>
	FG2 [†] [30]	3.96	2.23	7.03	<u>1.84</u>	<u>4.81</u>	2.71	10.58	2.32
	Ours	3.12	1.28	<u>8.64</u>	2.63	4.04	<u>2.23</u>	<u>11.87</u>	3.03

Table 2. VIGOR test results. FG2[†] denotes our re-implementation, which achieves better performance than the originally reported results. For a fair comparison, **RANSAC is not applied to FG2. Best and second in bold and underline.**

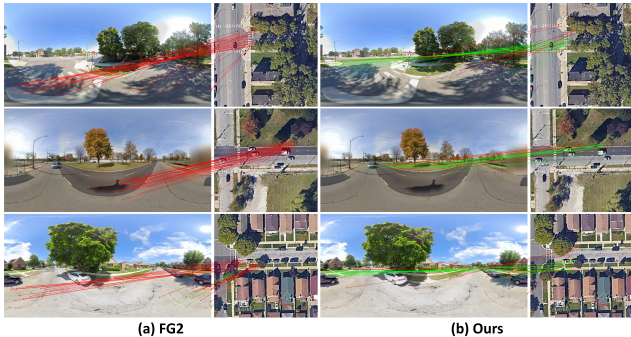


Figure 4. Cross-view image matching results on the CVFM benchmark. Green and red lines denote correct and incorrect matches.

and reliable cross-view correspondences.

Qualitative: The key strength of our method lies in its ability to perform accurate cross-view image matching. Large viewpoint changes introduce severe geometric distortions, and in some regions, only limited co-visible content exists. While methods like FG2 encode visual information in the BEV space and attempt to establish correspondences there, it remains difficult and unreliable to directly match ground-view and aerial-view features. Our approach addresses this by incorporating surface modeling, which provides geometric constraints that guide the establishment of physically consistent correspondences across views.

As shown in Fig. 4, we visualize top-30 matches produced by FG2 appear visually correct but are in fact incorrect when validated on the proposed CVFM benchmark. In contrast, our method yields substantially more reliable correspondences, significantly reducing false matches.

4.4. Results on cross-view localization

Quantitative: We evaluate our method against state-of-the-art cross-view localization approaches on the VIGOR and DReSS-D datasets, as reported in Tab. 2 and Tab. 3, respectively. In the Known Orientation setting. Our method consistently achieves the lowest mean and median localization errors on both datasets, showing that the proposed modules significantly enhance cross-view localization. The small performance gap between the cross-view and same-view scenarios further highlights the potential of our approach for real-world deployment.

In the more challenging Unknown Orientation setting. Our method delivers the best localization accuracy, outperforming the closest competitor (FG2) by substantial margins—up to 0.8m on VIGOR and 1.0m on DReSS-D in mean error. For orientation accuracy, our method is slightly behind FG2 by less than 3° on average, while still achieving the lowest overall mean loss. Notably, our re-implementation of FG2 (denoted FG2[†]) yields significantly better results than those originally reported, and all comparisons are made against this stronger baseline for fairness.

Qualitative: Fig. 5 compares FG2 and our method on the VIGOR dataset for cross-view localization. For each method, the leftmost column shows the height map derived from the ground-view image, with indices 0–10 corresponding to real-world heights from −10 m to 10 m. Inaccurate height estimation in (a) leads to mismatches, highlighted in red boxes. A shared region is marked in yellow across views for visual comparison.

FG2 does not estimate true surface height but selects an unconstrained feature-layer index along the height dimension. When this index is incorrect, BEV grids may sample features from wrong regions in the ground-view image, leading to semantic misalignment and unstable BEV repre-

Orient.	Methods	Same-area				Cross-area			
		Localization (m)		Orientation (°)		Localization (m)		Orientation (°)	
		Mean	Median	Mean	Median	Mean	Median	Mean	Median
Known	CCVPE [32]	2.83	0.98	-	-	5.91	1.87	-	-
	FG2 [†] [30]	<u>1.73</u>	<u>0.76</u>	-	-	<u>2.70</u>	1.53	-	-
	Slice-Loc [37]	2.10	0.82	-	-	3.99	<u>1.52</u>	-	-
	Ours	1.64	0.73	-	-	2.65	1.42	-	-
Unknown	CCVPE [32]	<u>3.01</u>	1.02	14.44	7.94	6.05	2.23	37.39	10.27
	FG2 [†] [30]	4.07	1.99	8.34	1.53	<u>5.23</u>	3.12	10.33	2.14
	Ours	2.93	<u>1.49</u>	<u>8.59</u>	<u>1.58</u>	4.24	<u>2.39</u>	<u>13.47</u>	<u>2.68</u>

Table 3. DReSS-D test results. FG2[†] denotes our re-implementation. **RANSAC is not applied. Best and second in bold and underline.**

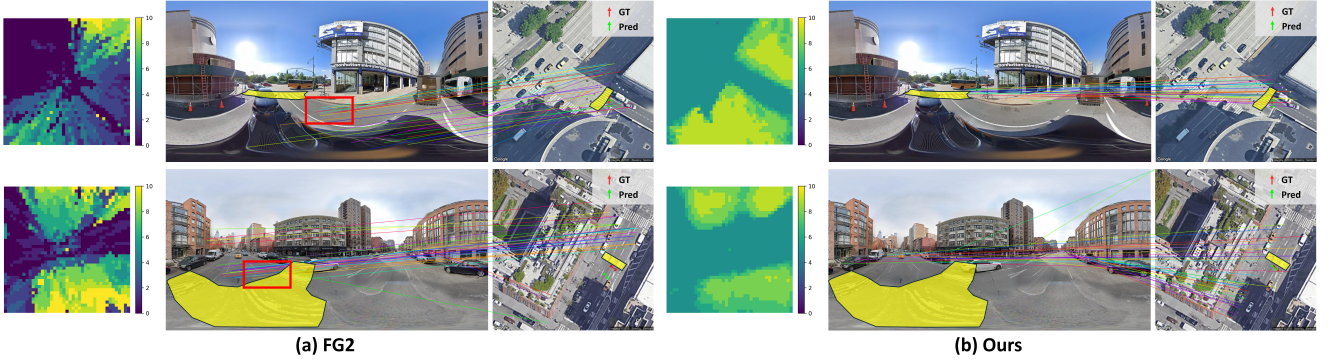


Figure 5. Visualization of cross-view localization for (a) FG2 and (b) our method. Shared regions are highlighted in yellow across views

sentations. The mismatches marked in red illustrate such errors. Our method explicitly predicts visible surface height, ensuring each BEV grid retrieves features from the correct physical region, producing geometrically consistent BEV features and improving localization accuracy.

Methods	Same-area (m)		Cross-area (m)	
	Mean	Median	Mean	Median
base	2.16	1.03	2.67	1.48
w/ Surface Model	2.09	1.04	2.36	1.37
w/ SimRefiner	2.09	1.00	2.37	1.36
Ours	1.92	0.96	2.27	1.32

Table 4. Ablations on proposed modules in VIGOR Known orientation setting. **Best in bold.**

4.5. Ablation study

We evaluate the contribution of each proposed module on the VIGOR dataset under the known-orientation setting, with results summarized in Tab. 4. The baseline model (base) follows the BEV-based localization pipeline without our proposed enhancements. Adding the Surface Model yields consistent improvements in both same-area and cross-area scenarios, as more reliable BEV features are

constructed by sampling only from geometrically valid regions in the ground view. Integrating the SimRefiner alone also enhances performance by refining the BEV similarity matrix, suppressing mismatches, and reinforcing structural consistency. Combining both modules achieves the best results, demonstrating their complementary effects: the Surface Model strengthens the geometric fidelity of BEV features, while the SimRefiner improves matching reliability.

5. Conclusion

We revisited cross-view localization from the perspective of image matching, emphasizing that accurate cross-view correspondence is critical for localization in extreme viewpoint disparities. To this end, we proposed a unified framework with two key modules: the Surface Model, which grounds BEV construction on estimated surface geometry, and SimRefiner, which refines similarity matrices by enforcing local and global consistency without costly post-processing. The components improve both localization and cross-view matching. Beyond method, we introduced CVFM, the first large-scale benchmark with dense pixel-level cross-view correspondences, enabling evaluation of matching algorithms. This work bridges localization and matching, enabling unified, geometry-aware cross-view understanding.

References

- [1] Eduardo Arnold, Jamie Wynn, Sara Vicente, Guillermo Garcia-Hernando, Aron Monszpart, Victor Prisacariu, Daniyar Turmukhambetov, and Eric Brachmann. Map-free visual relocalization: Metric pose relative to a single image. In *European Conference on Computer Vision*, pages 690–708. Springer, 2022. 5
- [2] Axel Barroso-Laguna, Sowmya Munukutla, Victor Adrian Prisacariu, and Eric Brachmann. Matching 2d images in 3d: Metric relative pose from metric correspondences. In *Proceedings of the IEEE/CVF Conference on Computer Vision and Pattern Recognition*, pages 4852–4863, 2024. 2, 3
- [3] Fabian Deuser, Konrad Habel, and Norbert Oswald. Sample4geo: Hard negative sampling for cross-view geolocalisation. In *Proceedings of the IEEE/CVF International Conference on Computer Vision*, pages 16847–16856, 2023. 2
- [4] Johan Edstedt, Qiyu Sun, Georg Bökman, Mårten Wadenbäck, and Michael Felsberg. Roma: Robust dense feature matching. In *Proceedings of the IEEE/CVF Conference on Computer Vision and Pattern Recognition*, pages 19790–19800, 2024. 2, 3
- [5] Weiwei Fan, Xinyi Liu, Yongjun Zhang, Dong Wei, Haoyu Guo, and Dongdong Yue. 3d wireframe model reconstruction of buildings from multi-view images using neural implicit fields. *Automation in Construction*, 174:106145, 2025. 3
- [6] Florian Fervers, Sebastian Bullinger, Christoph Bodensteiner, Michael Arens, and Rainer Stiefelhausen. Uncertainty-aware vision-based metric cross-view geolocalization. In *Proceedings of the IEEE/CVF Conference on Computer Vision and Pattern Recognition*, pages 21621–21631, 2023. 2
- [7] Ted Lentsch, Zimin Xia, Holger Caesar, and Julian FP Kooij. Slicematch: Geometry-guided aggregation for cross-view pose estimation. In *Proceedings of the IEEE/CVF Conference on Computer Vision and Pattern Recognition*, pages 17225–17234, 2023. 2, 7
- [8] Vincent Leroy, Yohann Cabon, and Jérôme Revaud. Grounding image matching in 3d with mast3r. In *European Conference on Computer Vision*, pages 71–91. Springer, 2024. 2, 3
- [9] Hao Li, Fabian Deuser, Wenping Yin, Xuanshu Luo, Paul Walther, Gengchen Mai, Wei Huang, and Martin Werner. Cross-view geolocalization and disaster mapping with street-view and vhr satellite imagery: A case study of hurricane ian. *ISPRS Journal of Photogrammetry and Remote Sensing*, 220:841–854, 2025. 1
- [10] Zhiqi Li, Wenhai Wang, Hongyang Li, Enze Xie, Chonghao Sima, Tong Lu, Qiao Yu, and Jifeng Dai. Bevformer: learning bird’s-eye-view representation from lidar-camera via spatiotemporal transformers. *IEEE Transactions on Pattern Analysis and Machine Intelligence*, 2024. 4, 6
- [11] Yi Liu, Xinyi Liu, Panwang Xia, Qiong Wu, Yi Wan, and Yongjun Zhang. Stereoinr: Cross-view geometry consistent stereo super resolution with implicit neural representation. *arXiv preprint arXiv:2505.05509*, 2025. 3
- [12] Will Maddern, Geoffrey Pascoe, Chris Linegar, and Paul Newman. 1 year, 1000 km: The oxford robotcar dataset. *The International Journal of Robotics Research*, 36(1):3–15, 2017. 1
- [13] Ben Mildenhall, Pratul P Srinivasan, Matthew Tancik, Jonathan T Barron, Ravi Ramamoorthi, and Ren Ng. Nerf: Representing scenes as neural radiance fields for view synthesis. *Communications of the ACM*, 65(1):99–106, 2021. 3
- [14] Maxime Oquab, Timothée Darcet, Théo Moutakanni, Huy Vo, Marc Szafraniec, Vasil Khalidov, Pierre Fernandez, Daniel Haziza, Francisco Massa, Alaaeldin El-Nouby, et al. Dinov2: Learning robust visual features without supervision. *arXiv preprint arXiv:2304.07193*, 2023. 3
- [15] Paul-Edouard Sarlin, Daniel DeTone, Tomasz Malisiewicz, and Andrew Rabinovich. Superglue: Learning feature matching with graph neural networks. In *Proceedings of the IEEE/CVF conference on computer vision and pattern recognition*, pages 4938–4947, 2020. 2, 3
- [16] Yujiao Shi and Hongdong Li. Beyond cross-view image retrieval: Highly accurate vehicle localization using satellite image. In *Proceedings of the IEEE/CVF Conference on Computer Vision and Pattern Recognition*, pages 17010–17020, 2022. 2
- [17] Yujiao Shi, Liu Liu, Xin Yu, and Hongdong Li. Spatial-aware feature aggregation for image based cross-view geolocalization. *Advances in Neural Information Processing Systems*, 32, 2019. 2
- [18] Yujiao Shi, Xin Yu, Liu Liu, Dylan Campbell, Piotr Koniusz, and Hongdong Li. Accurate 3-dof camera geo-localization via ground-to-satellite image matching. *IEEE transactions on pattern analysis and machine intelligence*, 45(3):2682–2697, 2022. 2
- [19] Yujiao Shi, Fei Wu, Akhil Perincherry, Ankit Vora, and Hongdong Li. Boosting 3-dof ground-to-satellite camera localization accuracy via geometry-guided cross-view transformer. In *Proceedings of the IEEE/CVF International Conference on Computer Vision*, pages 21516–21526, 2023. 2
- [20] Yujiao Shi, Hongdong Li, Akhil Perincherry, and Ankit Vora. Weakly-supervised camera localization by ground-to-satellite image registration. In *European Conference on Computer Vision*, pages 39–57. Springer, 2024.
- [21] Zhenbo Song, Jianfeng Lu, Yujiao Shi, et al. Learning dense flow field for highly-accurate cross-view camera localization. *Advances in Neural Information Processing Systems*, 36:70612–70625, 2023. 2, 7
- [22] Jiaming Sun, Zehong Shen, Yuang Wang, Hujun Bao, and Xiaowei Zhou. Loftr: Detector-free local feature matching with transformers. In *Proceedings of the IEEE/CVF conference on computer vision and pattern recognition*, pages 8922–8931, 2021. 2, 3
- [23] Khiem Vuong, Anurag Ghosh, Deva Ramanan, Srinivasa Narasimhan, and Shubham Tulsiani. Aerialmegadepth: Learning aerial-ground reconstruction and view synthesis. In *Proceedings of the Computer Vision and Pattern Recognition Conference*, pages 21674–21684, 2025. 3, 6
- [24] Shuzhe Wang, Vincent Leroy, Yohann Cabon, Boris Chidlovskii, and Jerome Revaud. Dust3r: Geometric 3d vi-

- sion made easy. In *Proceedings of the IEEE/CVF Conference on Computer Vision and Pattern Recognition*, pages 20697–20709, 2024. 2, 3
- [25] Xiaolong Wang, Runsen Xu, Zhuofan Cui, Zeyu Wan, and Yu Zhang. Fine-grained cross-view geo-localization using a correlation-aware homography estimator. *Advances in Neural Information Processing Systems*, 36:5301–5319, 2023. 2, 7
- [26] Qiong Wu, Yi Wan, Zhi Zheng, Yongjun Zhang, Guangshuai Wang, and Zhenyang Zhao. Camp: A cross-view geo-localization method using contrastive attributes mining and position-aware partitioning. *IEEE Transactions on Geoscience and Remote Sensing*, 2024. 2
- [27] Qiong Wu, Panwang Xia, Lei Yu, Yi Liu, Mingtao Xiong, Liheng Zhong, Jingdong Chen, Ming Yang, Yongjun Zhang, and Yi Wan. Cross-view image set geo-localization. *arXiv preprint arXiv:2412.18852*, 2024.
- [28] Panwang Xia, Yi Wan, Zhi Zheng, Yongjun Zhang, and Jiwei Deng. Enhancing cross-view geo-localization with domain alignment and scene consistency. *IEEE Transactions on Circuits and Systems for Video Technology*, 2024.
- [29] Panwang Xia, Lei Yu, Yi Wan, Qiong Wu, Peiqi Chen, Liheng Zhong, Yongxiang Yao, Dong Wei, Xinyi Liu, Lixiang Ru, et al. Cross-view geo-localization with panoramic street-view and vhr satellite imagery in decentrality settings. *ISPRS Journal of Photogrammetry and Remote Sensing*, 227:1–11, 2025. 2, 6
- [30] Zimin Xia and Alexandre Alahi. Fg²: Fine-grained cross-view localization by fine-grained feature matching. In *Proceedings of the Computer Vision and Pattern Recognition Conference*, pages 6362–6372, 2025. 2, 3, 4, 5, 6, 7, 8
- [31] Zimin Xia, Olaf Booij, Marco Manfredi, and Julian FP Kooij. Visual cross-view metric localization with dense uncertainty estimates. In *European Conference on Computer Vision*, pages 90–106. Springer, 2022. 2
- [32] Zimin Xia, Olaf Booij, and Julian FP Kooij. Convolutional cross-view pose estimation. *IEEE Transactions on Pattern Analysis and Machine Intelligence*, 46(5):3813–3831, 2023. 2, 7, 8
- [33] Zimin Xia, Yujiao Shi, Hongdong Li, and Julian FP Kooij. Adapting fine-grained cross-view localization to areas without fine ground truth. In *European Conference on Computer Vision*, pages 397–415. Springer, 2024. 2
- [34] Lihe Yang, Bingyi Kang, Zilong Huang, Zhen Zhao, Xiaogang Xu, Jiashi Feng, and Hengshuang Zhao. Depth anything v2. *Advances in Neural Information Processing Systems*, 37:21875–21911, 2024. 4
- [35] Junyan Ye, Qiyao Luo, Jinhua Yu, Huaping Zhong, Zhimeng Zheng, Conghui He, and Weijia Li. Sg-bev: satellite-guided bev fusion for cross-view semantic segmentation. In *Proceedings of the IEEE/CVF Conference on Computer Vision and Pattern Recognition*, pages 27748–27757, 2024. 1
- [36] Dongdong Yue, Xinyi Liu, Yi Wan, Yongjun Zhang, Maoteng Zheng, Weiwei Fan, and Jiachen Zhong. Nerfortho: Orthographic projection images generation based on neural radiance fields. *International Journal of Applied Earth Observation and Geoinformation*, 136:104378, 2025. 3
- [37] Yongjun Zhang, Mingtao Xiong, Yi Wan, and Gui-Song Xia. Cross-view localization via redundant sliced observations and a-contrario validation. *arXiv preprint arXiv:2508.05369*, 2025. 2, 6, 8
- [38] Sijie Zhu, Taojiannan Yang, and Chen Chen. Vigor: Cross-view image geo-localization beyond one-to-one retrieval. In *Proceedings of the IEEE/CVF Conference on Computer Vision and Pattern Recognition*, pages 3640–3649, 2021. 6
- [39] Xizhou Zhu, Weijie Su, Lewei Lu, Bin Li, Xiaogang Wang, and Jifeng Dai. Deformable detr: Deformable transformers for end-to-end object detection. *arXiv preprint arXiv:2010.04159*, 2020. 4